J Mater Sci (2019) 54:14742–14751

Composites & nanocomposites

Broadband photodetection of 2D Bi_2O_2Se–$MoSe_2$ heterostructure

Tao Yang[1], Xing Li[1,*], Liming Wang[2], Yiming Liu[1], Kaijian Chen[1], Xun Yang[1], Lei Liao[2], Lin Dong[1,*], and Chong-Xin Shan[1,*]

[1] Henan Key Laboratory of Diamond Optoelectronic Materials and Devices, School of Physics and Engineering, Zhengzhou University, Zhengzhou 450052, China

[2] School of Physics and Electronics, Hunan University, Changsha 410082, China

Received: 23 May 2019
Accepted: 22 August 2019
Published online: 3 September 2019

ABSTRACT

Due to their unique structure and photoelectrical properties, two-dimensional (2D) materials have attracted enormous attention on next-generation optoelectronic devices. Recently, the newly discovered 2D layered Bi_2O_2Se has exhibited outstanding sensitivity and optoelectronic properties. However, the performance of these 2D layered Bi_2O_2Se photodetectors can be limited by the high dark currents. The suitable band structure of 2D $MoSe_2$ can form a type-II heterojunction with Bi_2O_2Se, which can reduce the dark current, modulate the interlayer transition energy and induce the charge spatial separation. Herein, we demonstrated a photodetector based on the heterojunction fabricated by van der Waals assembly between Bi_2O_2Se and few-layer $MoSe_2$, showing visible to near-infrared detection range. Moreover, our results showed that the dark current of this photodetector was significantly reduced and the I_{on}/I_{off} ratio was greatly improved. Importantly, it exhibited a broad detection range from 405 to 808 nm with a responsivity of 413.1 mA W^{-1}, a high detectivity of 3.7×10^{11} Jones (at 780 nm) at room temperature. Compared with the 2D Bi_2O_2Se photodetector, the photocurrent response and recovery time in the heterojunction photodetector was greatly reduced from 1.92/1.31 to 0.79/0.49 s at room temperature. Our results showed that 2D $Bi_2O_2Se/MoSe_2$ heterojunction has a great potential for broadband and fast photodetection.

Introduction

During the past decades, two-dimensional (2D) materials have attracted enormous attention for photodetection applications due to their layered structure, mechanical flexibility, layer-dependent electronic band structures and easily constructed heterostructures [1–5]. Generally, the ideal detectors should have fast respond, high sensitivity and air stability, which are rare to meet at the same time in one material [6–12]. As the most extensively studied

Address correspondence to E-mail: xingli@zzu.edu.cn; ldong@zzu.edu.cn; cxshan@zzu.edu.cn

https://doi.org/10.1007/s10853-019-03963-1

2D material, graphene shows a relatively low optical absorption coefficient due to the lack of a band gap [13–15]. Though MoS_2 has shown good properties in optoelectronic applications, the corresponding photodetectors only respond to the visible region, leading to limitation of their application in the infrared region [16–18]. As an analog to graphene, black phosphorus with a direct bandgap also shows promising applications in photodetectors, while it is not stable in the air [19–21]. Due to the availability of 2D materials with various bandgaps and work functions, bandgap engineering of heterostructures can be realized through heterogeneous stacks built by different 2D materials, providing solutions for multifunctional hybrid photodetectors [22–25].

As a new type of 2D semiconductor, Bi_2O_2Se has been reported to possess high mobility and superior air stability [26]. Bi_2O_2Se consists alternative compensating cations ($(Bi_2O_2)_n^{2n+}$) and anions (Se_n^{2n-}). The layers are held together by weak electrostatic forces with an interlayer spacing of about 0.608 nm (Fig. 1a) [27]. However, the high dark current and small on/off ratio limit the performance of the photodetector based on Bi_2O_2Se on f-mica substrate [28, 29]. It has been reported that the Type-II heterojunction can reduce the dark current, modulate the interlayer transition energy and induce the charge spatial separation [30–34]. The Bi_2O_2Se typically exhibits an indirect band gap of $\sim$ 1.14 eV and the monolayer $MoSe_2$ exhibit a direct bandgap of $\sim$ 1.51 eV [35–37]. Therefore, 2D $MoSe_2$ can form a type-II van der Waals heterostructure with Bi_2O_2Se, which is quite promising for the performance improvement in Bi_2O_2Se-based photodetectors [38–40].

Here, we constructed a type-II $Bi_2O_2Se/MoSe_2$ van der Waals heterojunction and investigated the photodetection performance. Compared with the 2D Bi_2O_2Se photodetector, the dark current was significantly reduced and the on/off ratio was greatly improved in the Bi_2O_2Se–$MoSe_2$ heterostructure. Moreover, the Bi_2O_2Se–$MoSe_2$ based photodetector showed a broadband photoresponsivity from visible (405 nm) to near-infrared (808 nm) light illumination. Compared with the 2D Bi_2O_2Se photodetector, the photocurrent response and recovery time were greatly reduced in the heterojunction photodetector. Under the illumination of 780 nm laser, the heterojunction showed a responsivity of 413.1 mA W^{-1} and a detectivity of 3.7×10^{11} Jones at 2 V voltage.

Experimental section

Synthesis of 2D Bi_2O_2Se

The 2D Bi_2O_2Se crystals were synthesized through chemical vapor deposition method (CVD) in a dual zone split tube furnace (OTF-1200X, Hefei Kejing Material Technology Company Ltd., China) equipped with a 40-mm-diameter quartz tube. Typically, the source materials of Bi_2O_3 powder (aladdin, 99.99%) and Bi_2Se_3 power (aladdin, 99.99%) were placed in the center and upstream by 5 cm of high-temperature zone, respectively. The freshly cleaved fluorophlogopite mica ($[KMg_3(AlSi_3O_{10})F_2]$) was placed in the center of low-temperature zone as the target growth substrate (Fig. 1b). High-purity Ar gas was used as the carrier gas with a constant flow rate of 300 sccm and the pressure was kept at 0.3 atm. The whole reaction process was carried out under the furnace temperature of 640 °C and 540 °C and the growth was maintained for 30-60 min. Then, the furnace was naturally cooled down to the room temperature.

Characterization

The morphology of the as-grown Bi_2O_2Se was characterized by optical microscopy (OM, Olympus BX51 M microscope). The X-ray diffraction (XRD, X'Pert Powder PANalytical B.V.) was used to confirm the lattice structure of the 2D Bi_2O_2Se. The atomic force microscopy (AFM, AIST-NT) was used to investigate the thickness of 2D Bi_2O_2Se crystals. The element valence state of 2D Bi_2O_2Se crystals was characterized by X-ray photoelectron spectroscopy (XPS, AXIS Supra). Raman spectra were collected with a confocal Raman spectrometer (LabRAM HR Evolution) using a He–Ne laser (633 nm). The as-synthesized samples were transferred onto the copper grid supported lacey carbon film by using a HF-etched transfer method and the crystal structure was characterized by transmission electron microscopy (TEM, JEOL 2100) [26, 41].

Device preparation

The $Bi_2O_2Se/MoSe_2$ heterojunctions were achieved through a polymethyl methacrylate (PMMA)-mediated transfer method. Firstly, the PMMA (450 K, Suzhou Research Semiconductor Company Ltd.,

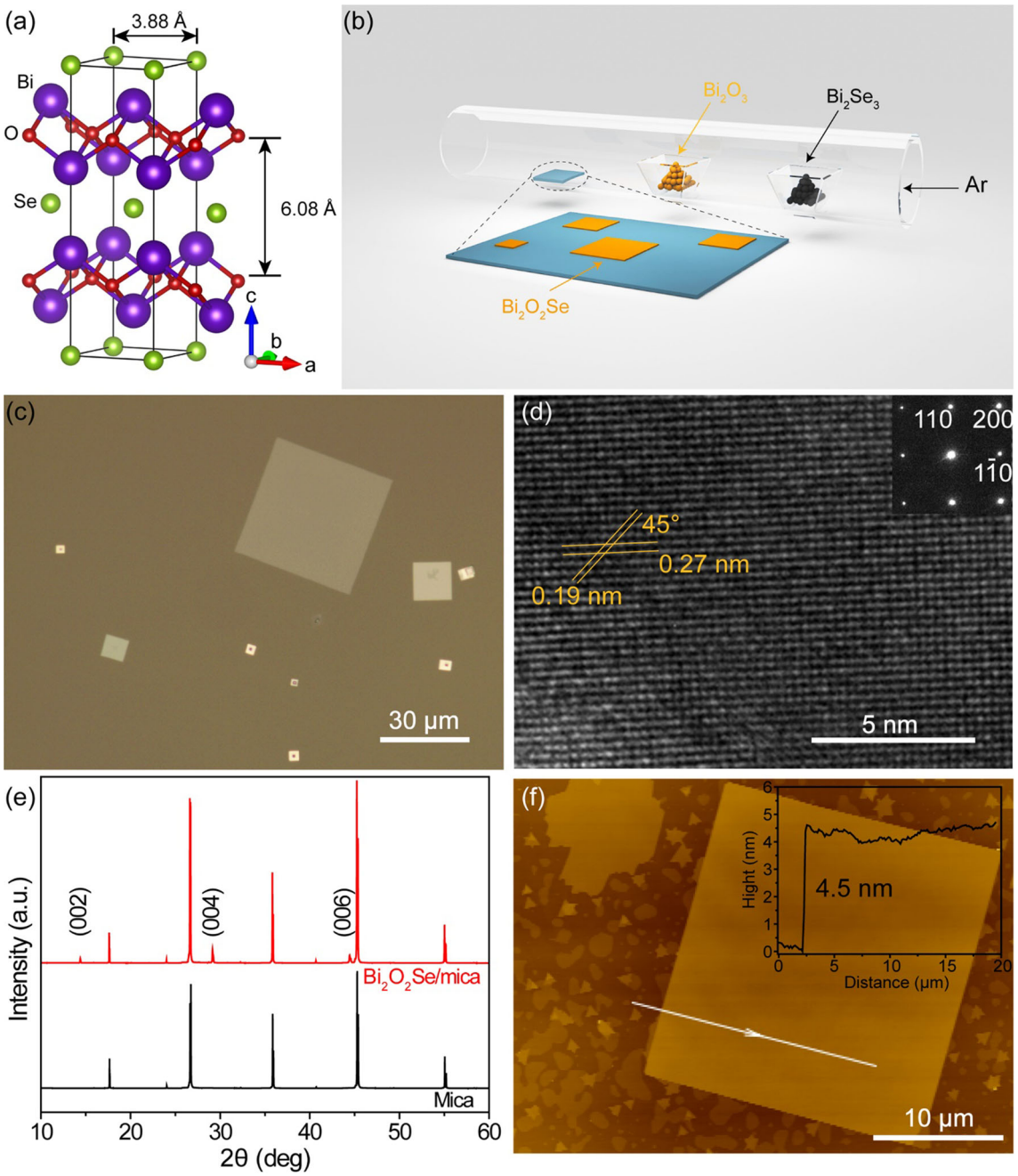

Figure 1 Characterization of Bi_2O_2Se nanoplates. **a** Schematic illustration of the crystal structure of Bi_2O_2Se with tetragonal structure. **b** Schematic illustration of the experimental setup for the synthesis of Bi_2O_2Se nanoplates. **c** Typical OM image of the as-synthesized 2D Bi_2O_2Se nanoplates on mica. **d** HRTEM image of the Bi_2O_2Se nanoplate. The inset shows a SAED pattern of the Bi_2O_2Se nanoplate. **e** XRD spectra of Bi_2O_2Se nanoplates grown on mica (red) and a reference mica substrate (black). **f** The AFM image of a Bi_2O_2Se nanoplate. The inset shows the thickness of this Bi_2O_2Se nanoplate is 4.5 nm from the AFM cross-sectional profile along the white line.

China.) was spin-coated over 2D $MoSe_2$ grown on SiO_2/Si substrates (Shenzhen 6Carbon Technology Company Ltd.) and baked at 80–90 °C for 15 min to facilitate intimate adhesion of the PMMA layer with $MoSe_2$. After that, the SiO_2/Si substrate was etched in 2.5 mol L^{-1} NaOH solution to separate the PMMA/$MoSe_2$ with the Si substrate. After several washes in the deionized (DI) water, the PMMA-$MoSe_2$ film was then transferred onto the mica substrate with grown 2D Bi_2O_2Se. After baking at 110 °C for 30 min, the

PMMA was finally removed with acetone and the mica substrate was cleaned with alcohol and DI water. The metallic contacts for the $Bi_2O_2Se/MoSe_2$ heterojunction were fabricated by standard electron beam lithography, thermal deposition of Cr/Au (10 nm/50 nm), and lift-off processes.

Optoelectronic measurements

The electrical measurements were performed using Lake Shore CPX probe station and Keithley 4200 semiconductor characterization system. The excitation laser wavelengths used in this paper were 405 nm, 515 nm, 660 nm, 780 nm and 808 nm.

Results and discussion

Single crystalline 2D Bi_2O_2Se samples were synthesized through a low-pressure CVD method. According to the OM image (Fig. 1c), Bi_2O_2Se nanoplates up to 40 μm with square morphology were obtained, indicating the tetragonal structure of Bi_2O_2Se. The corresponding high-resolution transmission electron microscopy (HRTEM) image in Fig. 1d indicates the single crystallinity and tetragonal structure of our synthesized Bi_2O_2Se nanoplates, which is also confirmed by the selected area electron diffraction (SAED) pattern (insert in Fig. 1d). As indicated in the HRTEM, d-spacing of 0.27 nm and 0.19 nm correspond, respectively, to the (200) and (110) planes with angle of 45°. The XRD spectrum (Fig. 1e) peaks of 14.39°, 29.15°, 44.44° correspond to the (002), (004) and (006) diffractions of tetragonal Bi_2O_2Se. According to the AFM image shown in Fig. 1f, the surface of the as-grown sample is homogeneous and the thickness is about 4.5 nm, which corresponds to a seven-layer sample.

The CVD synthesized 2D $MoSe_2$ (Shenzhen 6Carbon Technology Company Ltd.) generally showed a thickness of 1.3 nm (Fig. S1(a)). The HRTEM image and corresponding SAED pattern (Fig. S1(b)) showed the single crystallinity of the synthesized $MoSe_2$. With PMMA-assisted transfer method, the $Bi_2O_2Se/MoSe_2$ heterojunctions were constructed by transferring $MoSe_2$ directly onto the as-grown Bi_2O_2Se on mica (Fig. 2a). Due to the inertness of f-mica and strong electrostatic interaction between the Bi_2O_2Se with the substrate, hydrofluoric acid (HF) becomes the only f-mica etchant which can help the transfer of $Bi_2O_2Se/MoSe_2$ from the f-mica to the TEM grid. However, as a component of typical buffered oxide etchant, Bi_2O_2Se can be inevitably etched by HF during the transfer process. Therefore, the Raman spectroscopy was performed to further verify the $Bi_2O_2Se/MoSe_2$ heterojunction. Figure 2b shows the corresponding Raman spectra for $MoSe_2$ and Bi_2O_2Se obtained from point 1 and point 2 in Fig. 2a, where the A_{1g} (240 cm^{-1}), E^1_{2g} (280 cm^{-1}) mode of $MoSe_2$ and A_{1g} (160 cm^{-1}) mode of Bi_2O_2Se can be observed. The Raman intensity mappings of the white framed area in Fig. 2a with the A_{1g} mode of $MoSe_2$ at 240 cm^{-1} (Fig. 2c) and A_{1g} mode of Bi_2O_2Se at 160 cm^{-1} (Fig. 2d) show clearly the formation of the $Bi_2O_2Se/MoSe_2$ heterojunction (Fig. 2e).

In order to study the photoresponse performance of the $Bi_2O_2Se/MoSe_2$ heterojunction, two-terminal devices were fabricated and the schematic illustration of this device is presented in Fig. 3a. Figure 3b shows the $I-V$ curves of the photodetector in dark and under light illuminations with various wavelengths. According to our results, it can be seen that the photodetector experienced a remarkable current increase under light illuminations and the I_{on}/I_{off} ratios at 2 V bias voltage are 17.89, 746.45, 434.58, 218.01 and 60.25 when illuminated by lasers with wavelength of 405 nm (0.2 mW cm^{-2}), 515 nm (40.9 mW cm^{-2}), 660 nm (114.1 mW cm^{-2}), 780 nm (1197.1 mW cm^{-2}) and 808 nm (32.47 mW cm^{-2}). When compared with the performance of our synthesized pure Bi_2O_2Se (Fig. S2 in the supporting information), the dark current was significantly lowered (2.1 pA *vs.* 150 pA) and the I_{on}/I_{off} ratio was greatly improved (746.45 *vs.* 20.28 at 515 nm) through the construction of $Bi_2O_2Se/MoSe_2$ heterojunction.

To quantify the effect of light intensity on the device performance, the $I-V$ characteristics of the $Bi_2O_2Se/MoSe_2$ heterojunction photodetector were measured under illumination of 780 nm laser with power intensities ranging from dark to 1191.7 mW cm^{-2}. The responsivity (R) and specific detectivity (D^*) of this photodetector can be obtained based on the following equations [42–46]:

$$R(\mathrm{A\ W^{-1}}) = \frac{I_{ph}}{P_{opt} \cdot S}$$

$$D^*(\mathrm{Jones}) = \frac{\sqrt{A} \cdot R}{\sqrt{2eI_D}}$$

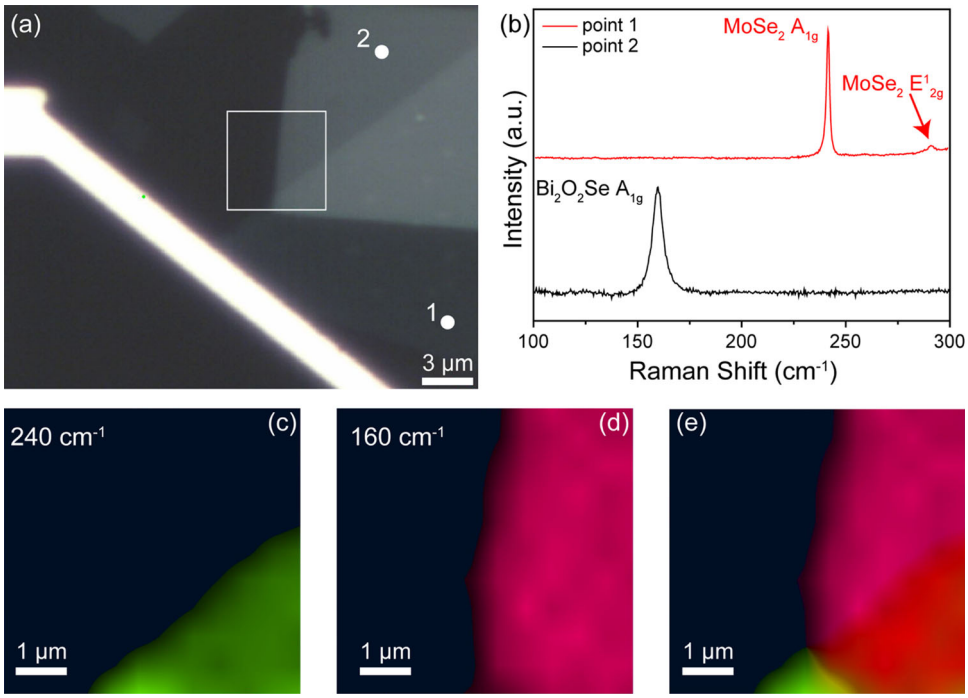

Figure 2 Raman spectroscopy analysis of the $Bi_2O_2Se/MoSe_2$ heterojunction. **a** The OM image of a $Bi_2O_2Se/MoSe_2$ heterojunction. **b** The Raman spectra taken from points 1 and 2 in **a**, showing pristine $MoSe_2$ and Bi_2O_2Se areas, respectively. The Raman intensity mappings at **c** 240 cm^{-1} (A_{1g} mode of $MoSe_2$) and **d** 160 cm^{-1} (A_{1g} mode of Bi_2O_2Se). **e** The superposition of **c** and **d**.

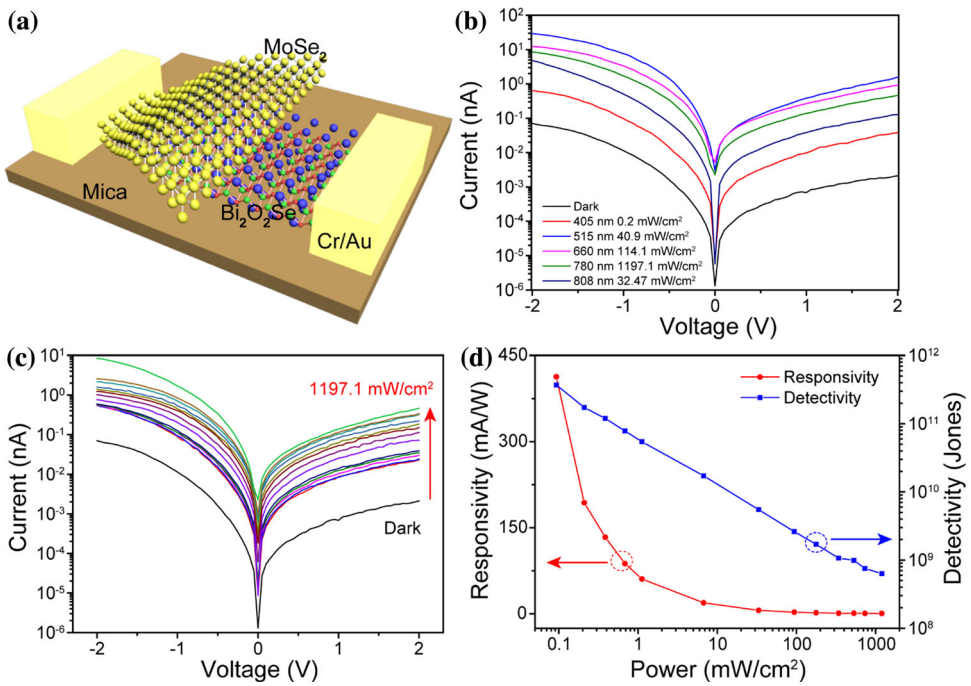

Figure 3 **a** Schematic illustration of the $Bi_2O_2Se/MoSe_2$ heterojunction photodetector. **b** $I-V$ characteristics of the photodetector in dark and under illumination of lasers with wavelength of 405, 515, 660, 780, and 808 nm, respectively. **c** $I-V$ characteristics of the $Bi_2O_2Se/MoSe_2$ heterojunction photodetector under illumination of 780 nm laser with various laser intensities. **d** Responsivity and detectivity of the $Bi_2O_2Se/MoSe_2$ heterojunction photodetector under illumination of 780 nm laser with different power at 2 V bias.

where P_{opt}, S, A, e, and I_D are light intensity, irradiation area, device area, unit charge, and dark current, respectively. The responsivity and detectivity as a function of light intensities (780 nm) are presented in Fig. 3d. Both the responsivity and the detectivity decrease with the increasing light intensities, and

reach 413.1 mA W^{-1} and 3.7 × 10^{11} Jones (1 Jones = 1 cm $Hz^{1/2}$ W^{-1}) under the intensity of 0.09 mW cm^{-2}.

The $I-V$ curves under light illumination with different wavelengths revealed that the Bi_2O_2Se/$MoSe_2$ heterojunction photodetector has a broad photoresponse from 405 to 808 nm (Fig. 3b). Therefore, the photoresponse properties of Bi_2O_2Se/$MoSe_2$ heterojunction photodetector to incident light with different wavelengths were further investigated. As shown in Fig. 4a–e, the photodetector exhibited stable and repeatable photoresponse to lasers with wavelengths of 405 nm (0.2 mW cm^{-2}), 515 nm (40.9 mW cm^{-2}), 660 nm (114.1 mW cm^{-2}), 780 nm (1197.1 mW cm^{-2}) and 808 nm (32.47 mW cm^{-2}) under bias of 1.5 V, indicating that Bi_2O_2Se/$MoSe_2$ heterojunction photodetector can response to light signals with a wide spectrum range from visible to NIR.

The response speed of the Bi_2O_2Se/$MoSe_2$ heterojunction photodetector was evaluated by analyzing the rising and falling edges of individual response cycle (Fig. S4). The response time was calculated to be 0.79/0.49 s under illumination of 515 nm with power intensity of 40.9 mW cm^{-2} at 1.5 V bias. Compared with the 2D Bi_2O_2Se photodetector (Fig. S3), the photocurrent response and recovery time was greatly reduced in the heterojunction photodetector. The device performances of the Bi_2O_2Se/$MoSe_2$ heterojunction photodetector and some recently reported 2D material-based photodetectors are summarized in Table 1. According to the summarized date, our reported Bi_2O_2Se/$MoSe_2$ heterojunction photodetector show higher detectivity and the measured rise/decay time is closely comparable to the values reported for many 2D materials-based photodetectors [47–58]. Moreover, the Bi_2O_2Se/$MoSe_2$ heterojunction show higher responsivity than other 2D material-based heterojunctions like CuO/MoS_2, MoS_2/$MoTe_2$, MoS_2/graphene *etc.* [47–51] It has been reported that the longer rise and decay time observed in similar systems can be attributed to unavoidable intrinsic and/or extrinsic charge traps, e.g., surface states and atmospheric contamination [59, 60]. In our devices, the heterojunction was fabricated by transferring $MoSe_2$ onto Bi_2O_2Se through a PMMA-assisted method, which can inevitably introduce undesired contamination at the interface between Bi_2O_2Se and $MoSe_2$ [36]. The chemical residues left on the surface of active materials during the removal of PMMA will form undesired charge impurities [22]. Moreover, the etching process with NaOH to separate the PMMA/$MoSe_2$ with the Si substrate may also introduce some chemical degradations on the $MoSe_2$ layers, resulting

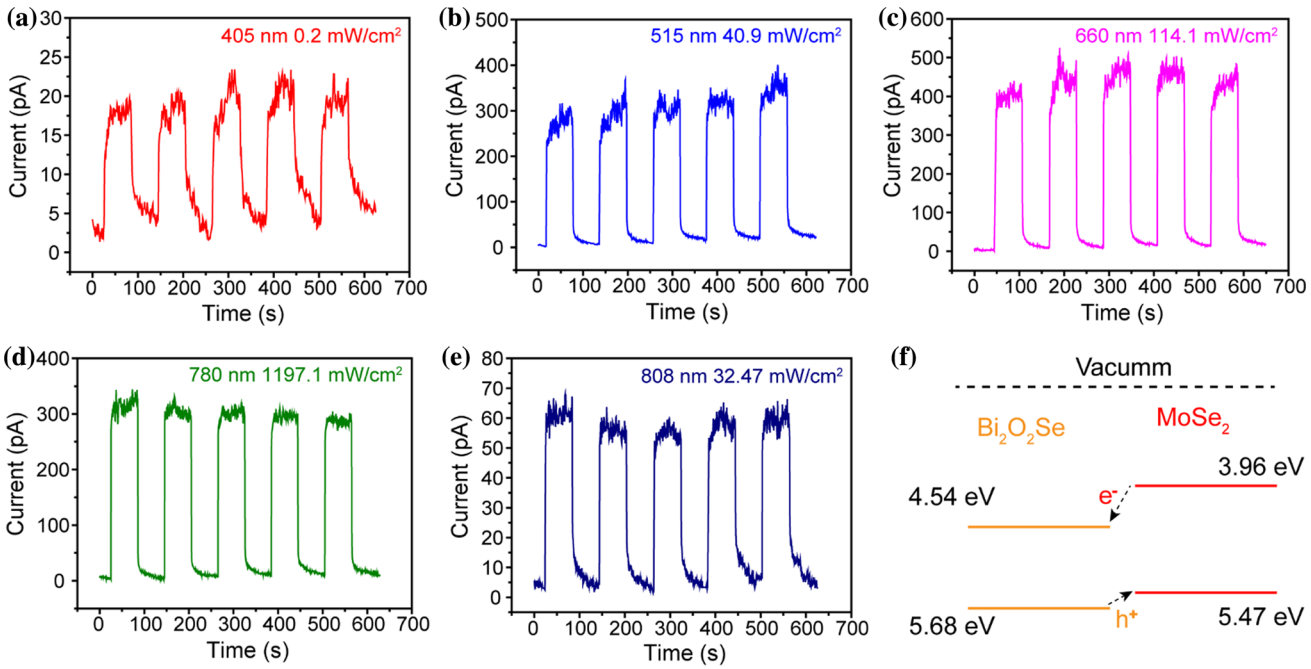

Figure 4 **a**–**e** Time-dependent photoresponse of Bi_2O_2Se/$MoSe_2$ heterojunction photodetector at 1.5 V voltage under illumination of 405, 515, 660, 780, and 808 nm laser, respectively. **f** Schematic illustration of the energy band diagrams for the Bi_2O_2Se/$MoSe_2$ heterojunction.

Table 1 2D material-based photodetectors and performance comparison with our results

Material	λ (nm)	R (A W^{-1})	D (Jones)	Rise/decay time (s)	References
$Bi_2O_2Se/MoSe_2$	780	0.413	3.7×10^{11}	0.79/0.49 (515 nm)	This work
CuO/MoS_2	532	0.011	3.27×10^{8}	–	[47]
$MoS_2/MoTe_2$	473	0.047	1.6×10^{10}	0.385/—	[48]
MoS_2/graphene	405	0.014	–	–	[49]
$ReS_2/ReSe_2$	550	0.021	–	0.4/0.4	[50]
ZnO/WS_2	340	0.002	–	5.7/2.6	[51]
SnS_2	375	1.42	1.38×10^{10}	0.307/7.9	[52]
Bi_2Te_3	325	26.82	1.29×10^{9}	0.28/1.6	[53]
Bi_2Te_3	1550	286	6.6×10^{9}	0.25/0.195	[54]
Bi_2Te_3	650	23.43	1.54×10^{10}	4.1/7.4	[55]
MoS_2	532	14	1.11×10^{10}	0.707/1.1	[56]
WS_2	532	5.8	–	1.5/1.5	[57]
WSe_2	635	0.92	–	0.9/2	[58]

in a relatively longer rise and decay time. Since the direct growth of 2D heterojunction will help us get a high-quality clean interface, growing $Bi_2O_2Se/MoSe_2$ heterostructures without a transferring method can help to further improve the corresponding photodetection performance of the $Bi_2O_2Se/MoSe_2$ system [61].

Figure 4f illustrates the alignment of electronic bands of Bi_2O_2Se and $MoSe_2$. It shows that the electron affinities of Bi_2O_2Se and $MoSe_2$ are 4.54 eV and 3.96 eV, the bandgaps are 1.14 eV and 1.51 eV, respectively. Consequently, the $Bi_2O_2Se/MoSe_2$ heterostructure forms a type-II heterojunction, with the conduction band minimum residing in Bi_2O_2Se and the valence band maximum in $MoSe_2$ [26, 35, 36]. In type-II heterojunctions, the conduction band minimum and valence band maximum reside in two separate materials. Photoexcited electrons and holes therefore prefer to stay at separate locations. As demonstrated in Fig. 4f, electron-hole pairs exist under the light illumination, and the electrons on the conduction band transfer from $MoSe_2$ to Bi_2O_2Se, while the holes on the valence band transfer from Bi_2O_2Se to $MoSe_2$, resulting in the efficient charge separation [62].

Conclusion

In conclusion, the 2D layered Bi_2O_2Se samples have been synthesized with low-pressure CVD method and the $Bi_2O_2Se/MoSe_2$ heterojunction with type-II band alignment was constructed for photodetection. Our results indicate that this heterojunction photodetector showed broadband detection ranging from visible (405 nm) to near infrared (808 nm) with a responsivity of 413.1 mA W^{-1}, detectivity of 3.7×10^{11} Jones (at 780 nm). Compared with the 2D Bi_2O_2Se photodetector, the dark current was significantly reduced and the I_{on}/I_{off} ratio was greatly improved. Importantly, the rise/decay time of the $Bi_2O_2Se/MoSe_2$ heterojunction photodetector was reduced from 1.92/1.31 to 0.79/0.49 s under the illumination of 515 nm (40.9 mW cm^{-2} at 1.5 V). Our results showed that 2D $Bi_2O_2Se/MoSe_2$ heterojunction has promising applications in the field of broadband and fast photodetection.

Acknowledgements

This work was supported by the National Science Foundation of China (Grant Nos. 11804304, 61804136) and China Postdoctoral Science Foundation (Grant No. 2017M622371).

Compliance with ethical standards

Conflict of interest The authors declare that they have no conflict of interest.

Electronic supplementary material: The online version of this article (https://doi.org/10.1007/s10853-019-03963-1) contains supplementary material, which is available to authorized users.

References

[1] Hu W, Yang JL (2017) Two-dimensional van der Waals heterojunctions for functional materials and devices. J Mater Chem C 5:12289–12297

[2] Xie LM (2015) Two-dimensional transition metal dichalcogenide alloys: preparation, characterization and applications. Nanoscale 7:18392–18401

[3] Yan FG, Wei ZM, Wei X, Lv QS, Zhu WK, Wang KY (2018) Toward high-performance photodetectors based on 2D materials: strategy on methods. Small Meth 2:1700349

[4] Tan CL, Cao XH, Wu XJ, He QY, Yang J, Zhang X, Chen JZ, Zhao W, Han SK, Nam GH, Sindoro M, Zhang H (2017) Recent advances in ultrathin two-dimensional nanomaterials. Chem Rev 117:6225–6331

[5] Wang XT, Cui Y, Li T, Lei M, Li JB, Wei ZM (2019) Recent advances in the functional 2D photonic and optoelectronic devices. Adv Opt Mater 7:1801274

[6] Buscema M, Island JO, Groenendijk DJ, Blanter SI, Steele GA, van der Zant HSJ, Castellanos-Gomez A (2015) Photocurrent generation with two-dimensional van der Waals semiconductors. Chem Soc Rev 44:3691–3718

[7] Hu PA, Wen ZZ, Wang LF, Tan PH, Xiao K (2012) Synthesis of few-layer GaSe nanosheets for high performance photodetectors. ACS Nano 6:5988–5994

[8] Sun ZH, Chang HX (2014) Graphene and graphene-like two-dimensional materials in photodetection: mechanisms and methodology. ACS Nano 8:4133–4156

[9] Tamalampudi SR, Lu YY, Kumar RU, Sankar R, Liao CD, Moorthy KB, Cheng CH, Chou FC, Chen YT (2014) High performance and bendable few-layered InSe photodetectors with broad spectral response. Nano Lett 14:2800–2806

[10] Zhang WJ, Chiu MH, Chen CH, Chen W, Li LJ, Wee ATS (2014) Role of metal contacts in high-performance phototransistors based on WSe_2 monolayers. ACS Nano 8:8653–8661

[11] Li X, Sun M, Shan CX, Chen Q, Wei XL (2018) Mechanical properties of 2D materials studied by in situ microscopy techniques. Adv Mater Interfaces 5:1701246

[12] Cheng S, Li J, Han MG, Deng SQ, Tan GT, Zhang XX, Zhu J, Zhu YM (2017) Topologically allowed nonsixfold vortices in a sixfold multiferroic material: observation and classification. Phys Rev Lett 118:145501

[13] Low T, Avouris P (2014) Graphene plasmonics for terahertz to mid-infrared applications. ACS Nano 8:1086–1101

[14] Jorgensen JH, Cabo AG, Balog R, Kyhl L, Groves MN, Cassidy AM, Bruix A, Bianchi M, Dendzik M, Arman MA, Lammich L, Ignacio Pascual J, Knudsen J, Hammer B, Hofmann P, Hornekaer L (2016) Symmetry-driven band gap engineering in hydrogen functionalized graphene. ACS Nano 10:10798–10807

[15] Xu XZ, Liu C, Sun ZH, Cao T, Zhang ZH, Wang E, Liu ZF, Liu KH (2018) Interfacial engineering in graphene bandgap. Chem Soc Rev 47:3059–3099

[16] Alkis S, Oztas T, Aygun LE, Bozkurt F, Okyay AK, Ortac B (2012) Thin film MoS_2 nanocrystal based ultraviolet photodetector. Opt Express 20:21815–21820

[17] Lopez-Sanchez O, Lembke D, Kayci M, Radenovic A, Kis A (2013) Ultrasensitive photodetectors based on monolayer MoS_2. Nat Nanotechnol 8:497–501

[18] Zhang WJ, Huang JK, Chen CH, Chang YH, Cheng YJ, Li LJ (2013) High-gain phototransistors based on a CVD MoS_2 monolayer. Adv Mater 25:3456–3461

[19] Chen PF, Li N, Chen XZ, Ong WJ, Zhao XJ (2018) The rising star of 2D black phosphorus beyond graphene: synthesis, properties and electronic applications. 2D Mater 5:014002

[20] Buscema M, Groenendijk DJ, Blanter SI, Steele GA, van der Zant HSJ, Castellanos-Gomez A (2014) Fast and broadband photoresponse of few-layer black phosphorus field-effect transistors. Nano Lett 14:3347–3352

[21] Engel M, Steiner M, Avouris P (2014) Black phosphorus photodetector for multispectral, high-resolution imaging. Nano Lett 14:6414–6417

[22] Chen XS, Qiu YF, Yang HH, Liu GB, Zheng W, Feng W, Cao WW, Hu WP, Hu P (2017) In-plane mosaic potential growth of large-area 2D layered semiconductors MoS_2-$MoSe_2$ lateral heterostructures and photodetector application. ACS Appl Mater Interfaces 9:1684–1691

[23] Zhang KN, Zhang TN, Cheng GH, Li TX, Wang SX, Wei W, Zhou XH, Yu WW, Sun Y, Wang P, Zhang D, Zeng CG, Wang XJ, Hu WD, Fan HJ, Shen GZ, Chen X, Duan XF, Chang K, Dai N (2016) Interlayer transition and infrared photodetection in atomically thin type-$MoTe_2$/MoS_2 van der Waals heterostructures. ACS Nano 10:3852–3858

[24] Um DS, Lee YS, Lim SD, Park S, Lee H, Koe H (2016) High-performance MoS_2/CuO nanosheet-on-one-dimensional heterojunction photodetectors. ACS Appl Mater Interfaces 8:33955–33962

[25] Liu KK, Li XM, Cheng SB, Zhou R, Liang YC, Dong L, Shan CX, Zeng HB, Shen DZ (2018) Carbon-ZnO alternating quantum dot chains: electrostatic adsorption assembly and white light-emitting device application. Nanoscale 10:7155–7162

[26] Wu JX, Yuan HT, Meng MM, Chen C, Sun Y, Chen ZY, Dang WH, Tan CW, Liu YJ, Yin JB, Zhou YB, Huang SY, Xu HQ, Cui Y, Hwang HY, Liu ZF, Chen YL, Yan BH, Peng HL (2017) High electron mobility and quantum oscillations

in non-encapsulated ultrathin semiconducting Bi_2O_2Se. Nat Nanotechnol 12:530–534

[27] Ruleova P, Drasar C, Lostak P, Li CP, Ballikaya S, Uher C (2010) Thermoelectric properties of Bi_2O_2Se. Mater Chem Phys 119:299–302

[28] Li J, Wang ZX, Wen Y, Chu JW, Yin L, Cheng RQ, Lei L, He P, Jiang C, Feng LP, He J (2018) High-performance near-infrared photodetector based on ultrathin Bi_2O_2Se nanosheets. Adv Funct Mater 28:1706437

[29] Tian XL, Luo HY, Wei RF, Zhu CH, Guo QY, Yang DD, Wang FQ, Li JF, Qiu JR (2018) An ultrabroadband mid-infrared pulsed optical switch employing solution-processed bismuth oxyselenide. Adv Mater 30:1801021

[30] Chen YC, Lu YJ, Lin CN, Tian YZ, Gao CJ, Dong L, Shan CX (2018) Self-powered diamond/β-Ga_2O_3 photodetectors for solar-blind imaging. J Mater Chem C 6:5727

[31] Hu H, Guo XD, Hu DB, Sun ZP, Yang XX, Dai Q (2018) Flexible and electrically tunable plasmons in graphene-mica heterostructures. Adv Sci 5:1800175

[32] Yang XX, Sun ZP, Low T, Hu H, Guo XD, Garcia de Abajo FJ, Avouris P, Dai Q (2018) Nanomaterial-based plasmon-enhanced infrared spectroscopy. Adv Mater 30:1704896

[33] Zhang WJ, Wang QX, Chen Y, Wang Z, Wee ATS (2016) Van der Waals stacked 2D layered materials for optoelectronics. 2D Mater 3:022001

[34] Cheng SB, Xu CS, Deng SQ, Han MG, Bao SY, Ma J, Nan CW, Duan WH, Bellaiche L, Zhu YM, Zhu J (2018) Interface reconstruction with emerging charge ordering in hexagonal manganite. Sci Adv 4:eaar4298

[35] Quhe R, Liu JC, Wu JX, Yang J, Wang YY, Li QH, Li TR, Guo Y, Yang JB, Peng HL, Lei M, Lu J (2018) High-performance sub-10 nm monolayer Bi_2O_2Se transistors. Nanoscale 11:532–540

[36] Gong YJ, Lei SD, Ye GL, Li B, He YM, Keyshar K, Zhang X, Wang QZ, Lou J, Liu Z, Vajtai R, Zhou W, Ajayan PM (2015) Two-step growth of two-dimensional $WSe_2/MoSe_2$ heterostructures. Nano Lett 15:6135–6141

[37] Li X, Sun M, Cheng SB, Ren XY, Zang JH, Xu TT, Wei XL, Li SF, Chen Q, Shan CX (2019) Crystallographic-orientation dependent Li ion migration and reactions in layered $MoSe_2$. 2D Mater 6:035027

[38] Shaw JC, Zhou HL, Chen Y, Weiss NO, Liu Y, Huang Y, Duan XF (2014) Chemical vapor deposition growth of monolayer $MoSe_2$ nanosheets. Nano Res 7:511–517

[39] Guo JH, Shi YT, Bai XG, Wang XC, Ma TL (2015) Atomically thin $MoSe_2$/Graphene and WSe_2/Graphene nanosheets for the highly efficient oxygen reduction reaction. J Mater Chem A 3:24397–24404

[40] Cheng S, Langelier B, Ra YH, Rashid RT, Mi Z, Botton GA (2019) Structural origin of the high-performance light-emitting InGaN/AlGaN quantum disks. Nanoscale 11:8994–8999

[41] Wu JX, Tan CW, Tan ZJ, Liu YJ, Yin JB, Dang WH, Wang MZ, Peng HL (2017) Controlled synthesis of high-mobility atomically thin bismuth oxyselenide crystals. Nano Lett 17:3021–3026

[42] Zhang ZD, Yang JH, Zhang K, Chen S, Mei FH, Shen GZ (2017) Anisotropic photoresponse of layered 2D SnS-based near infrared photodetectors. J Mater Chem C 5:11288–11293

[43] Abderrahmane A, Ko PJ, Jung PG, Kim NH, Sandhu A (2018) Optoelectronic characterizations of two-dimensional h-BN/$MoSe_2$ heterostructures based photodetector. Sci Adv Mater 10:627–631

[44] Wu D, Wang YG, Zeng LH, Jia C, Wu EP, Xu TT, Shi ZF, Tian YT, Li XJ, Tsang YH (2018) Design of 2D layered $PtSe_2$ heterojunction for the high-performance, room-temperature, broadband, infrared photodetector. ACS Photonics 5:3820–3827

[45] Shi ZF, Xu TT, Wu D, Zhang YT, Zhang BL, Tian YT, Li XJ, Du GT (2016) Semi-transparent all-oxide ultraviolet light-emitting diodes based on ZnO/NiO-core/shell nanowires. Nanoscale 8:9997–10003

[46] Zhang F, Shi ZF, Ma ZZ, Li Y, Li S, Wu D, Xu TT, Li X-J, Shan CX, Du GT (2018) Silica coating enhances the stability of inorganic perovskite nanocrystals for efficient and stable down-conversion in white light-emitting devices. Nanoscale 10:20131–20139

[47] Zhang K, Peng M, Wu W, Guo J, Gao G, Liu Y, Kou J, Wen R, Lei Y, Yu A, Zhang Y, Zhai J, Wang ZL (2017) A flexible p-CuO/n-MoS_2 heterojunction photodetector with enhanced photoresponse by the piezo-phototronic effect. Mater Horiz 4:274–280

[48] Wang F, Yin L, Wang ZX, Xu K, Wang FM, Shifa TA, Huang Y, Jiang C, He J (2016) Configuration-dependent electrically tunable van der Waals heterostructures based on $MoTe_2/MoS_2$. Adv Funct Mater 26:5499–5506

[49] Henck H, Pierucci D, Chaste J, Naylor CH, Avila J, Balan A, Silly MG, Asensio MC, Sirotti F, Johnson ATC, Lhuillier E, Ouerghi A (2016) Electrolytic phototransistor based on graphene-MoS_2 van der Waals p-n heterojunction with tunable photoresponse. Appl Phys Lett 109:113103

[50] Cho AJ, Namgung SD, Kim H, Kwon JY (2017) Electric and photovoltaic characteristics of a multi-layer $ReS_2/ReSe_2$ heterostructure. APL Mater 5:076101

[51] Lan C, Li C, Wang S, Yin Y, Guo H, Liu N, Liu Y (2016) ZnO-WS_2 heterostructures for enhanced ultra-violet photodetectors. RSC Adv 6:67520–67524

[52] Xu H, Xing J, Lu JH, Han X, Li D, Zhou Z, Bao LH, Gao HJ, Huang Y (2019) Annealing effects on the electrical and

photoelectric performance of SnS_2 field-effect transistor. Appl Surf Sci 484:39–44

[53] Sharma A, Srivastava AK, Senguttuvan TD, Husale S (2017) Robust broad spectral photodetection (UV-NIR) and ultra high responsivity investigated in nanosheets and nanowires of Bi_2Te_3 under harsh nano-milling conditions. Sci Rep 7:17911

[54] Sharma A, Senguttuvan TD, Ojha VN, Husale S (2019) Novel synthesis of topological insulator based nanostructures (Bi_2Te_3) demonstrating high performance photodetection. Sci Rep 9:3804

[55] Liu JL, Wang H, Li X, Chen H, Zhang ZK, Pan WW, Luo GQ, Yuan CL, Ren YL, Lei W (2019) High performance visible photodetectors based on thin two-dimensional Bi_2Te_3 nanoplates. J Alloys Compd 798:656–664

[56] Kumar R, Sharma A, Kaur M, Husale S (2017) Pt-nanostrip-enabled plasmonically enhanced broad spectral photodetection in bilayer MoS_2. Adv Opt Mater 5:1700009

[57] Ma X, Zhang R, An C, Wu S, Hu X, Liu J (2019) Efficient doping modulation of monolayer WS_2 for optoelectronic applications. Chin Phys B 28:037803

[58] Zheng Z, Zhang T, Yao J, Zhang Y, Xu J, Yang G (2016) Flexible, transparent and ultra-broadband photodetector based on large-area WSe_2 film for wearable devices. Nanotechnology 27:225501

[59] Ding Y, Zhou N, Gan L, Yan X, Wu R, Abidi IH, Waleed A, Pan J, Ou X, Zhang Q, Zhuang M, Wang P, Pan X, Fan Z, Zhai T, Luo Z (2018) Stacking-mode confined growth of 2H-$MoTe_2/MoS_2$ bilayer heterostructures for UV-vis-IR photodetectors. Nano Energy 49:200–208

[60] Mehew JD, Unal S, Torres Alonso E, Jones GF, Fadhil Ramadhan S, Craciun MF, Russo S (2017) Fast and highly sensitive ionic-polymer-gated WS_2-graphene photodetectors. Adv Mater 29:1700222

[61] Zhang Z, Gong Y, Zou X, Liu P, Yang P, Shi J, Zhao L, Zhang Q, Gu L, Zhang Y (2019) Epitaxial growth of two-dimensional metal-semiconductor transition-metal dichalcogenide vertical stacks (VSe_2/MX_2) and their band alignments. ACS Nano 13:885–893

[62] Kong WY, Wu GA, Wang KY, Zhang TF, Zou YF, Wang DD, Luo LB (2016) Graphene-β-Ga_2O_3 heterojunction for highly sensitive deep UV photodetector application. Adv Mater 28:10725–10731